

Large Tunneling Electroresistance, Tunneling Magnetoresistance, and Regulatable Negative Differential Conductance in a van der Waals Antiferroelectric Multiferroic Tunnel Junction


Yu Zhu^{1,2}, Boyuan Chi^{2,3}, Leina Jiang², Xiaoyan Guo¹, Yu Yan^{1,*} and Xiufeng Han^{2,3,4,†}

¹Key Laboratory of Physics and Technology for Advanced Batteries (Ministry of Education), Department of Physics, Jilin University, Changchun 130012, China

²Beijing National Laboratory for Condensed Matter Physics, Institute of Physics, Chinese Academy of Sciences, Beijing 100190, China

³Center of Materials Science and Optoelectronics Engineering, University of Chinese Academy of Sciences, Beijing 100049, China

⁴Songshan Lake Materials Laboratory, Dongguan, Guangdong 523808, China

 (Received 7 April 2023; revised 20 July 2023; accepted 8 August 2023; published 7 September 2023)

Multifunctional tunnel junction is a kind of electronic device and the emergence of van der Waals (vdW) materials provides a promising opportunity for the development of multifunctional tunnel junctions and the miniaturization of electronic devices beyond Moore's law. Here, we propose a symmetric vdW antiferroelectric multiferroic tunnel junction (AFMFTJ) based on $\text{Fe}_3\text{GeTe}_2/h\text{-BN}/\text{bilayer-In}_2\text{Se}_3/h\text{-BN}/\text{Fe}_3\text{GeTe}_2$ vdW heterostructure, and investigate the spin-dependent transport of this vdW AFMFTJ by using nonequilibrium Green's function combined with density-functional theory. It is found that multiple resistance states are realized in this proposed vdW AFMFTJ and the considerable tunneling electroresistance ratio of about $1.0 \times 10^4\%$ and the large tunneling magnetoresistance ratio of up to 695% are simultaneously achieved at zero bias. Interestingly, the regulatable negative differential conductance (NDC) by magnetic field and electric field is produced in this vdW AFMFTJ under bias voltages. The NDC effect originates from the changes in the conductive channels of Fe_3GeTe_2 electrodes and the electronic states of the In_2Se_3 barrier under different bias voltages. This work not only benefits exploring of the tunnel junction with NDC effect, but also provides a promising route for the design of multifunctional microelectronic devices based on vdW materials.

DOI: [10.1103/PhysRevApplied.20.034010](https://doi.org/10.1103/PhysRevApplied.20.034010)

I. INTRODUCTION

Based on the electron tunneling effect, a kind of electronic device known as tunnel junction has been developed, which is formed by sandwiching a thin insulating barrier layer between two metallic electrodes. As the well-studied tunnel junctions, magnetic tunnel junction (MTJ) and ferroelectric tunnel junction (FTJ) are widely used in spin valves [1,2], magnetic random-access memories [3], field-effect transistors [4,5], and resonant tunneling diodes [6,7]. As known, the tunneling magnetoresistance (TMR) effect of MTJ is the change in resistance of MTJ for parallel and antiparallel states of magnetization of the two ferromagnetic (FM) electrodes, and the tunneling electroresistance (TER) effect of FTJ comes from the variation of the tunnel resistance when the polarization of the

ferroelectric (FE) barrier is switched between two orientations. In general, it requires a distinct difference of two electrodes to achieve a large TER effect in FTJ. However, the different chemical potential of two electrodes in asymmetric FTJ will generate a strong built-in electric field, which prevents the reversal of FE polarization of the barrier. In recent years, the emergence of van der Waals (vdW) intrinsic magnets [8–10] and FE materials [11,12] offers exciting opportunities to design high-performance vdW tunnel junction based on vdW heterostructure [13–20]. Notably, it was theoretically predicted that the transitions between FE and antiferroelectric (AFE) states can result in the large change of transmission across symmetric antiferroelectric tunnel junction (AFTJ) with a vdW AFE barrier sandwiched between two of the same electrodes by changing the barrier height, which can remove a strong built-in electric field induced by the different chemical potential of two electrodes in asymmetric FTJ [21]. In addition, by utilizing FM metal as electrodes in a FTJ or ferroelectric insulator as a barrier in a MTJ, four resistance

*yanyu@jlu.edu.cn

†xfhan@iphy.ac.cn

states with the TER and TMR effects can be realized in a single tunnel junction, which is named the multiferroic tunnel junction (MFTJ), thus holding attractive prospects in the application of multilevel memories and multifunctional spintronic devices. More recently, symmetric vdW antiferroelectric multiferroic tunnel junction (AFMFTJ) with a vdW antiferroelectric barrier sandwiched between the same vdW FM electrodes are theoretically proposed [22–24]. Compared to asymmetric FTJ, the obtained TER effect in the proposed symmetric vdW AFMFTJs are still small. For example, the reported TER ratio of symmetric vdW AFMFTJs based on Fe_3GeTe_2 /bilayer α - In_2Se_3 / Fe_3GeTe_2 and CrSe_2 / CuInP_2S_6 / CrSe_2 vdW heterostructures are only 744% and 90%, respectively [22,23]. It is therefore desirable to explore other symmetric vdW AFMFTJ to obtain the large TER and TMR ratios simultaneously.

Among the prepared vdW ferromagnetic metal, Fe_3GeTe_2 exhibits Curie temperature of about 220 K, high coercive field and perpendicular magnetic anisotropy [10,25]. In particular, the Curie temperature of exfoliated atomically thin Fe_3GeTe_2 can be increased to room temperature by an ionic gate, thus Fe_3GeTe_2 is a promising candidate for electrode material of next-generation vdW magnetic devices. On the other hand, vdW α - In_2Se_3 have been demonstrated to possess both out-of-plane and in-plane FE polarization at room temperature [26,27]. Furthermore, it was reported that head-to-head antiferroelectric (AFEH) state, tail-to-tail antiferroelectric (AFET) state and FE state can be achieved in bilayer In_2Se_3 and the transition barrier between these states is comparable to the FE switching barriers of typical bulk perovskite oxides, which means that bilayer α - In_2Se_3 is an ideal barrier material of the vdW AFMFTJ [21,23,26].

As one of the most fascinating tunneling phenomena of electronic devices, negative differential conductance (NDC) effect, has attracted a lot of attention due to its potential applications in fast switchers, high-frequency oscillators, logic circuits, and amplifiers [28–31]. Though it has been seen in a variety of systems [32–36], the tunneling-based NDC have not yet been reported in the vdW AFMFTJ and MFTJ

Driven by these motivations, we propose a symmetric vdW AFMFTJ based on Fe_3GeTe_2 / h -BN/bilayer- In_2Se_3 / h -BN/ Fe_3GeTe_2 vdW heterostructure (FGT/BN/IS/BN/FGT vdW AFMFTJ), and investigate the spin-dependent transport as well as the TMR and TER effects of this vdW AFMFTJ by using nonequilibrium Green's function (NEGF) with density-functional theory (DFT). Our calculations reveal that the multiple resistive states with considerable TER ratio and large TMR ratio are realized in this vdW AFMFTJ due to different configurations of the magnetic moment in two Fe_3GeTe_2 electrodes and the different states of the dipole ordering in the In_2Se_3 barrier. Furthermore, the regulatable NDC by magnetic field and

electric field is produced in this vdW AFMFTJ under bias voltages.

II. METHODS

The calculations for structure optimization were performed by the Vienna *ab initio* simulation package (VASP) [37,38]. Generalized gradient approximation (GGA) with the Perdew-Burke-Ernzerhof (PBE) version was adopted for the exchange-correlation potential [39,40]. The vdW interactions of two-dimensional materials was treated by the optB86b exchange functional [41]. A plane-wave energy cutoff of 500 eV and a $7 \times 7 \times 1$ Monkhorst-Pack k -point grid were used for the structural optimization. The convergence criteria for energy and force were set to be 1×10^{-6} eV and 0.01 eV/Å. A vacuum space of 15 Å was used to avoid the spurious interaction between periodic replicas.

The calculations of electronic structure and transport properties were performed using the Nanocal package based on the nonequilibrium Green's function (NEGF) combined with the DFT [42,43]. The spin-resolved conductance G_σ of the FGT/BN/IS/BN/FGT vdW AFMFTJ is calculated using the Landauer-Büttiker formula:

$$G_\sigma = \frac{e^2}{h} \sum_{k_\parallel} T_\sigma(k_\parallel, E_F), \quad (1)$$

where e and h are the electron charge and the Planck constant, respectively. $T_\sigma(k_\parallel, E_F)$ is the transmission coefficient with spin σ ($\sigma = \uparrow, \downarrow$) at the Fermi level E_F and transverse Bloch wave vector k_\parallel ($k_\parallel = k_x, k_y$). The spin-resolved transmission coefficient with spin σ is calculated using the NEGF formalism

$$T_\sigma = \text{Tr}[\Gamma_{1,\sigma} G_\sigma^r \Gamma_{2,\sigma} G_\sigma^a], \quad (2)$$

where G_σ^r (G_σ^a) is the retarded (advanced) Green's function of the scattering region. $\Gamma_{1,\sigma}$ ($\Gamma_{2,\sigma}$) is defined as

$$\Gamma_{m,\sigma} = i[\Sigma_{m,\sigma}^r - \Sigma_{m,\sigma}^a], \quad (m = 1, 2), \quad (3)$$

where $\Sigma_{m,\sigma}^r$ ($\Sigma_{m,\sigma}^a$) represent the retarded (advanced) self-energy of the electrode m ($m=1, 2$).

At bias voltage V , the spin-resolved current across the FGT/BN/IS/BN/FGT vdW AFMFTJ is calculated as follows:

$$I_\sigma = \frac{e}{h} \int_{\mu_2}^{\mu_1} T_\sigma(E, V) [f_1(E) - f_2(E)] dE, \quad (4)$$

where $T_\sigma(E, V)$ is the transmission coefficient with spin σ at energy E with spin σ under the applied bias voltage V , $f_1(E)$ ($f_2(E)$) is the Fermi distribution function of

electrons in electrode 1 (electrode 2), and μ_1 (μ_2) is the electrochemical potential of electrode 1 (electrode 2).

The cutoff energy of 80 Hartree and the double- ζ atomic orbital basis were used for the transport calculations. A $11 \times 11 \times 1$ k mesh was used for self-consistent calculations. The convergence criterion of the Hamiltonian matrix and density matrix in the self-consistency were set to be 1×10^{-4} eV. The energy interval in the current calculation was set as 5×10^{-3} eV. The k points for the spin-resolved transmission coefficient and current calculations were $150 \times 150 \times 1$. Considering the accuracy and amount of calculation, $31 \times 31 \times 1$ and $150 \times 150 \times 1$ k meshes were adopted, respectively, for the calculation of density of states of bilayer In_2Se_3 of the vdW AFMFTJ and conductive channels of Fe_3GeTe_2 electrodes in the two-dimensional Brillouin zone (2DBZ).

III. RESULTS AND DISCUSSIONS

In agreement with the previous computational and experimental values, the optimized in-plane lattice constants of bulk Fe_3GeTe_2 , bilayer In_2Se_3 , and monolayer h -BN are 4.00, 4.08, and 2.54 Å, respectively [44–47]. In order to construct the FGT/BN/IS/BN/FGT vdW AFMFTJ with the minimal lattice mismatch, $\sqrt{3} \times \sqrt{3}$ unit cell of h -BN and 1×1 unit cell of bilayer In_2Se_3 are used to model barriers and 1×1 unit cell of Fe_3GeTe_2 is adopted to model electrodes. Figure 1 shows the structure of the FGT/BN/IS/BN/FGT vdW AFMFTJ for the AFEH, AFET, and FE states, in which the vdW AFMFTJ is divided into semi-infinite left and right Fe_3GeTe_2 electrodes and a central scattering region and the central scattering region is a bilayer Fe_3GeTe_2 /monolayer BN/bilayer In_2Se_3 /monolayer h -BN/bilayer Fe_3GeTe_2 (FGT/BN/IS/BN/FGT) vdW heterostructure. The in-plane lattice constant of the FGT/BN/IS/BN/FGT vdW heterostructure is set as the lattice constant of unit cell of bulk Fe_3GeTe_2 , thus bilayer In_2Se_3 and monolayer h -BN in the FGT/BN/IS/BN/FGT vdW AFMFTJ are compressed by 2% and 8 %, respectively. As reported by Li *et al.*, 8% strain has little effect on the energy band of h -BN [48]. In order to examine the stability of FGT/BN/IS/BN/FGT vdW heterostructure, the binding energy of FGT/BN/IS/BN/FGT vdW heterostructure for three dipole ordering states is calculated using equation $E_b = (E_{ABC} - 2E_A - 2E_B - E_C)/N_{\text{atom}}$, where E_{ABC} , E_A , E_B and E_C represent the energies of FGT/BN/IS/BN/FGT vdW heterostructure, bilayer Fe_3GeTe_2 , monolayer BN and bilayer In_2Se_3 , respectively, and N_{atom} is the number of atoms in the vdW heterostructure. The calculated binding energies are -26.6 meV/atom, -25.0 meV/atom and -26.2 meV/atom for AFEH, AFET, and FE states, respectively, which indicates that the FGT/BN/IS/BN/FGT vdW heterostructure is stable enough to form the vdW AFMFTJ.

TABLE I. Calculated conductance (in units of e^2/h), TMR and TER ratios of the FGT/BN/IS/BN/FGT vdW AFMFTJ at zero bias voltage.

	AP	P	TMR (%)
AFEH	3.12×10^{-5}	2.42×10^{-4}	6.76×10^2
AFET	3.15×10^{-3}	3.17×10^{-3}	6.35×10^{-1}
FE	3.56×10^{-5}	2.83×10^{-4}	6.95×10^2
TER (%)	1.00×10^4	1.21×10^3	

Due to the antiparallel (AP) and parallel (P) configurations of the magnetic moment in two Fe_3GeTe_2 electrodes and the AFEH, AFET, and FE states of the dipole ordering in the In_2Se_3 barrier, multiple resistance states can be realized in the FGT/BN/IS/BN/FGT vdW AFMFTJ. The calculated conductance values of the vdW AFMFTJ for all resistance states are listed in Table I. The TMR ratio of this vdW AFMFTJ is defined as $\text{TMR} = (G_P - G_{AP})/G_{AP}$, where G_P and G_{AP} are the conductance of the P and AP configurations for each dipole ordering state, respectively. Also, the TER ratio at zero bias voltage is defined as $\text{TER} = (G_{\text{max}} - G_{\text{min}})/G_{\text{min}}$, where G_{max} and G_{min} are the maximum and minimum ones among conductance of the AFEH, AFET, and FE states for each magnetic configuration, respectively. It is seen from Table I that whether the magnetic moment of two electrodes is in the AP or P configuration, the conductance for the AFET state is significantly greater than that for the AFEH and FE states. Therefore, considerable TER ratio of $1.0 \times 10^4\%$ for the AP configuration and 1210% for the P configuration are achieved in the FGT/BN/IS/BN/FGT vdW AFMFTJ, which is much larger than the reported TER ratio of symmetric vdW AFMTJs based on Fe_3GeTe_2 /bilayer α - In_2Se_3 / Fe_3GeTe_2 and CrSe_2 / CuInP_2S_6 / CrSe_2 vdW heterostructures [22,23]. Meanwhile, the total conductance of the P configuration is obviously larger than that of the AP configuration in the AFEH and FE states, resulting in the large TMR ratio of up to 676% for the AFEH state and 695% for the FE state in the FGT/BN/IS/BN/FGT vdW AFMFTJ, respectively. In contrast, the conductance of the P configuration in the AFET state is very close to that of the AP configuration, thus the TMR ratio of the FGT/BN/IS/BN/FGT vdW AFMFTJ being very small.

As known, the electron transmission across the vdW AFMFTJ is closely related to the intrinsic conduction channels of FM Fe_3GeTe_2 electrodes and the electronic properties of bilayer In_2Se_3 barrier. Therefore, the difference in conductance of the vdW AFMFTJ for different resistance states can be clarified by analyzing these properties. Considering that the transmission of the FE state is similar to that of the AFEH state at zero bias voltage, we mainly clarify the transmission of the AFEH and AFET states below. The k -resolved density of states (DOS) of the In_2Se_3 barrier at the Fermi level in the two-dimensional

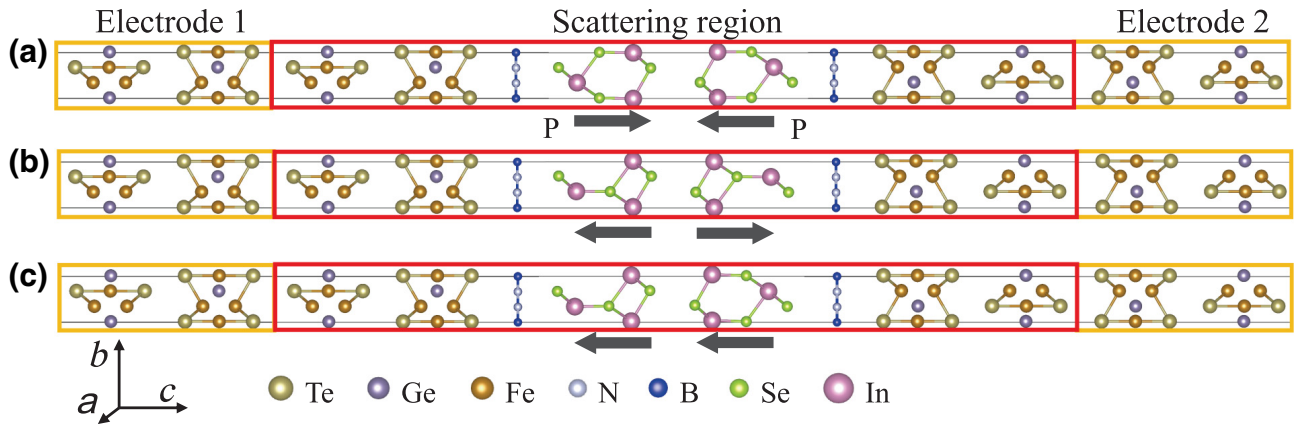


FIG. 1. Side view of the structure of the FGT/BN/IS/BN/FGT vdW AFMFTJ for (a) AFEH, (b) AFET, and (c) FE states. The black arrows indicate the polarization direction of In_2Se_3 layers.

Brillouin zone (2DBZ) for the AFEH and AFET states are shown in Figs. 2(a) and 2(b), respectively. As shown in Figs. 2(a) and 2(b), the electronic states of the In_2Se_3 barrier for the AFEH state mainly distribute at a narrow annular region of hexagon around the high-symmetry

Γ point of the 2DBZ, while those for the AFET state mainly concentrated in the small region centered at the Γ point, thus bilayer In_2Se_3 in the FGT/BN/IS/BN/FGT vdW heterostructure has slight metallicity. Figures 2(c) and 2(d) show the k -resolved majority-spin and minority-spin

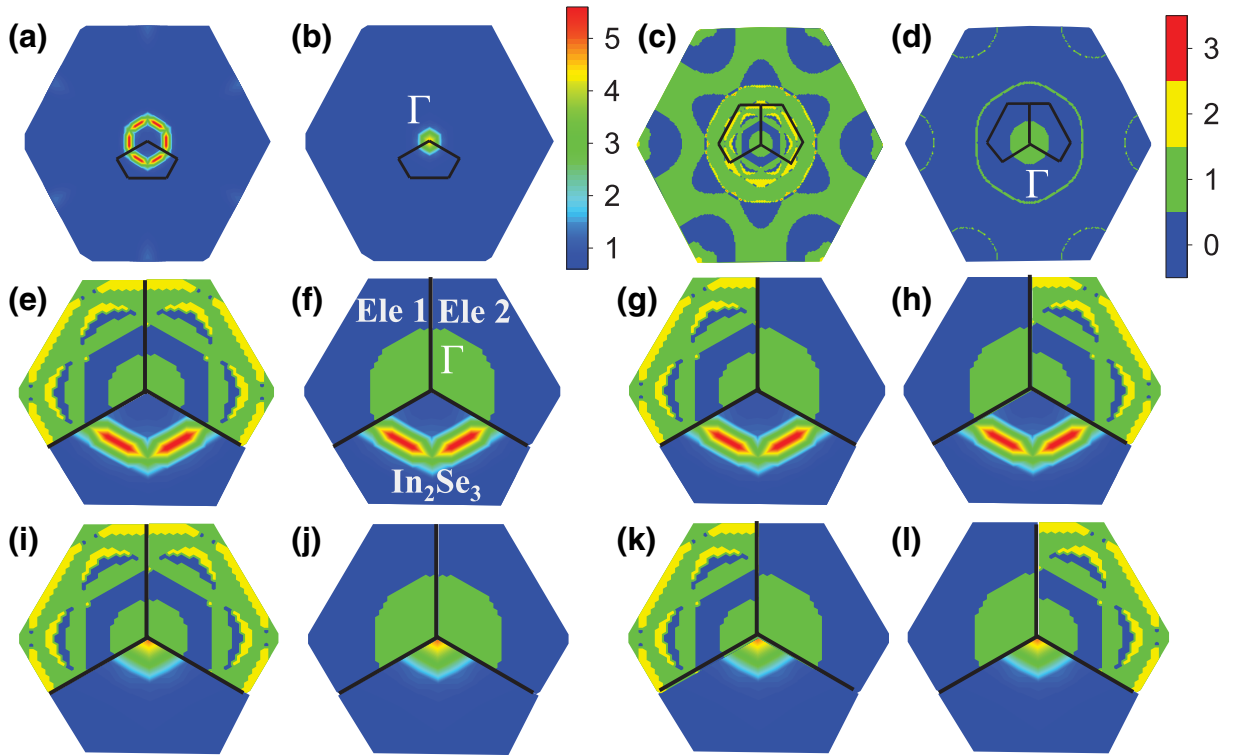


FIG. 2. k -resolved DOS of the In_2Se_3 barrier at the Fermi level in 2DBZ for (a) AFEH and (b) AFET states. k -resolved (c) majority-spin and (d) minority-spin conduction channels of Fe_3GeTe_2 electrode in the 2DBZ at the Fermi level. k -resolved (e) majority-spin and (f) minority-spin channels-DOS figure for the P configuration of the AFEH state. k -resolved (g) majority-spin and (h) minority-spin channels-DOS figure for the AP configuration of AFEH state. k -resolved (i) majority-spin and (j) minority-spin channels-DOS figure for the P configuration of the AFET state. k -resolved (k) majority-spin and (l) minority-spin channels-DOS figure for the AP configuration of AFET state. The color bar of DOS of the In_2Se_3 layer in channels-DOS figure is the same as that in (a),(b) and the color bar of conductive channels in channels-DOS figure is the same as that in (c),(d).

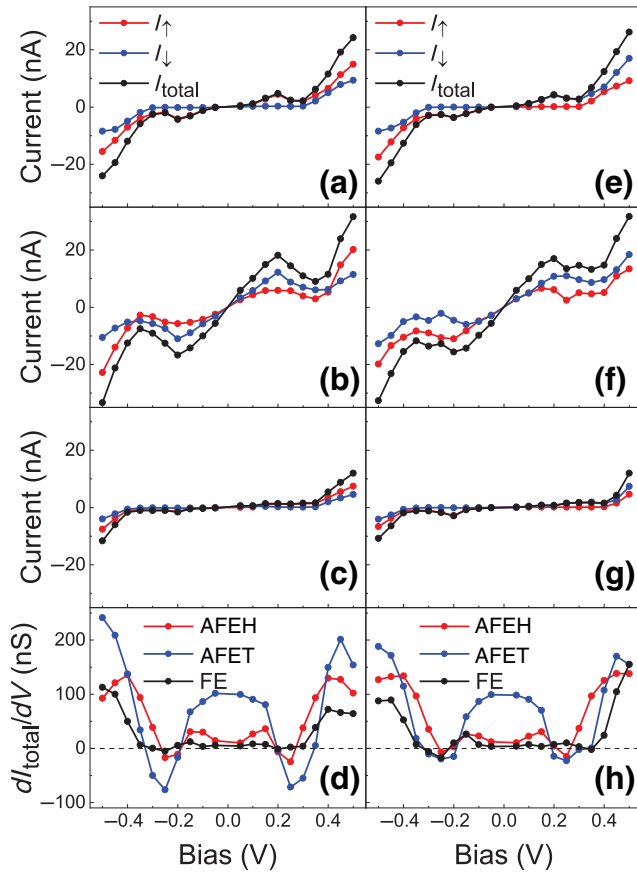


FIG. 3. Bias voltage dependences of currents of the P configuration of the FGT/BN/IS/BN/FGT vdW AFMFTJ for (a) AFEH, (b) AFET, and (c) FE states, respectively. Bias voltage dependences of currents of the AP configuration of the FGT/BN/IS/BN/FGT vdW AFMFTJ for (e) AFEH, (f) AFET, and (g) FE states, respectively. dI_{total}/dV spectra of total current for (d) P and (h) AP configurations. I_{\uparrow} , I_{\downarrow} , and I_{total} represent majority-spin, minority-spin and total currents, respectively.

conduction channels of Fe_3GeTe_2 electrode in the 2DBZ at the Fermi level, respectively. In order to facilitate the analysis of the transmission of electrons from electrode 1 (Ele 1) across the In_2Se_3 barrier into electrode 2 (Ele 2), we combine one repeating unit area of k -resolved majority or minority-spin conductive channel near the Γ point of Ele 1 [an area enclosed by black solid line in Figs. 2(c) and 2(d)], another repeating unit area of k -resolved majority or minority-spin conductive channel near the Γ point of Ele 2 [another area enclosed by black solid line in Figs. 2(c) and 2(d)] and the repeating unit area of k -resolved DOS near the Γ point of In_2Se_3 layer [the area enclosed by black solid line in Figs. 2(a) and 2(b)] to form k -resolved spin-dependence channels-DOS figure for each resistance state, in which the upper left and upper right parts are the majority or minority-spin conductive channels of Ele 1 and Ele 2, respectively, and the lower part is the DOS of the In_2Se_3 barrier, as shown in Figs. 2(e)–2(l).

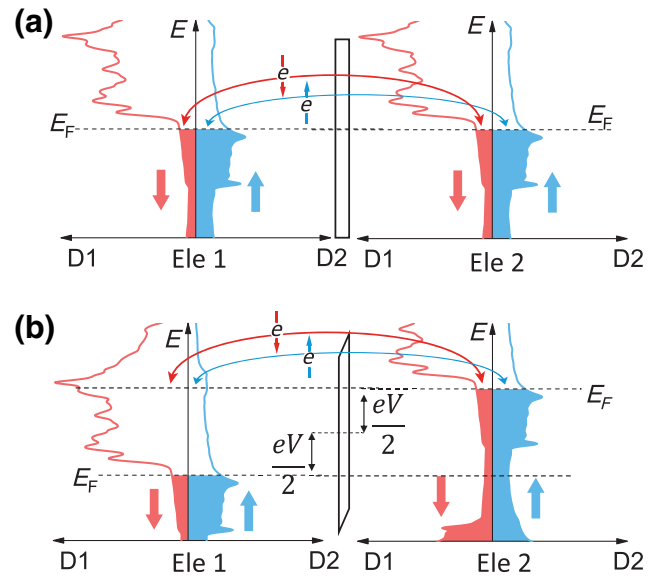


FIG. 4. Band alignments of two Fe_3GeTe_2 electrodes in the FGT/BN/IS/BN/FGT vdW AFMFTJ at (a) zero bias and (b) bias V when the magnetic moment of two electrodes is in the P configuration. Blue and red patterns represent majority-spin and minority-spin DOS of Fe_3GeTe_2 , respectively.

Figures 2(c) and 2(d) show that the Fe_3GeTe_2 electrode has the majority- and minority-spin conduction channels in the circular region centered at the Γ point. Meanwhile, the electronic states of the In_2Se_3 barrier for the AFET state mainly concentrated in the small region centered at the Γ point, supporting the metalliclike transmission across this area of In_2Se_3 for the AFET state. Consequently, the large electron transmission from Ele 1 across the In_2Se_3 barrier into Ele 2 can occur in the AFET state, whether the magnetic moment of two electrodes is in the AP or P configuration. In contrast, the electronic states of the In_2Se_3 barrier for the AFEH state mainly distribute at a narrow annular region of hexagon around the Γ point and the overlap of this annular region and the nonzero region of conductive channel of two electrodes is obviously smaller than that for the AFET state, as shown in Figs. 2(e)–2(l). Therefore, the transmission for the AFET state is significantly greater than that for the AFEH state, resulting in a considerable TER ratio. On the other hand, when the magnetic moment of two electrodes is in the AP configuration, the overlapping area between the annular region of electronic states of the In_2Se_3 barrier and the nonzero conductive channel of Ele 1 is obviously different from that between the annular region of electronic states of the In_2Se_3 barrier and the nonzero conductive channel of Ele 2 in the AFEH state due to different distribution of the majority and minority-spin conduction channels in the 2DBZ, as shown in Figs. 2(g) and 2(h), thus the transmission of the AP configuration is smaller than that of the P configuration in the AFEH state since the spin and transverse

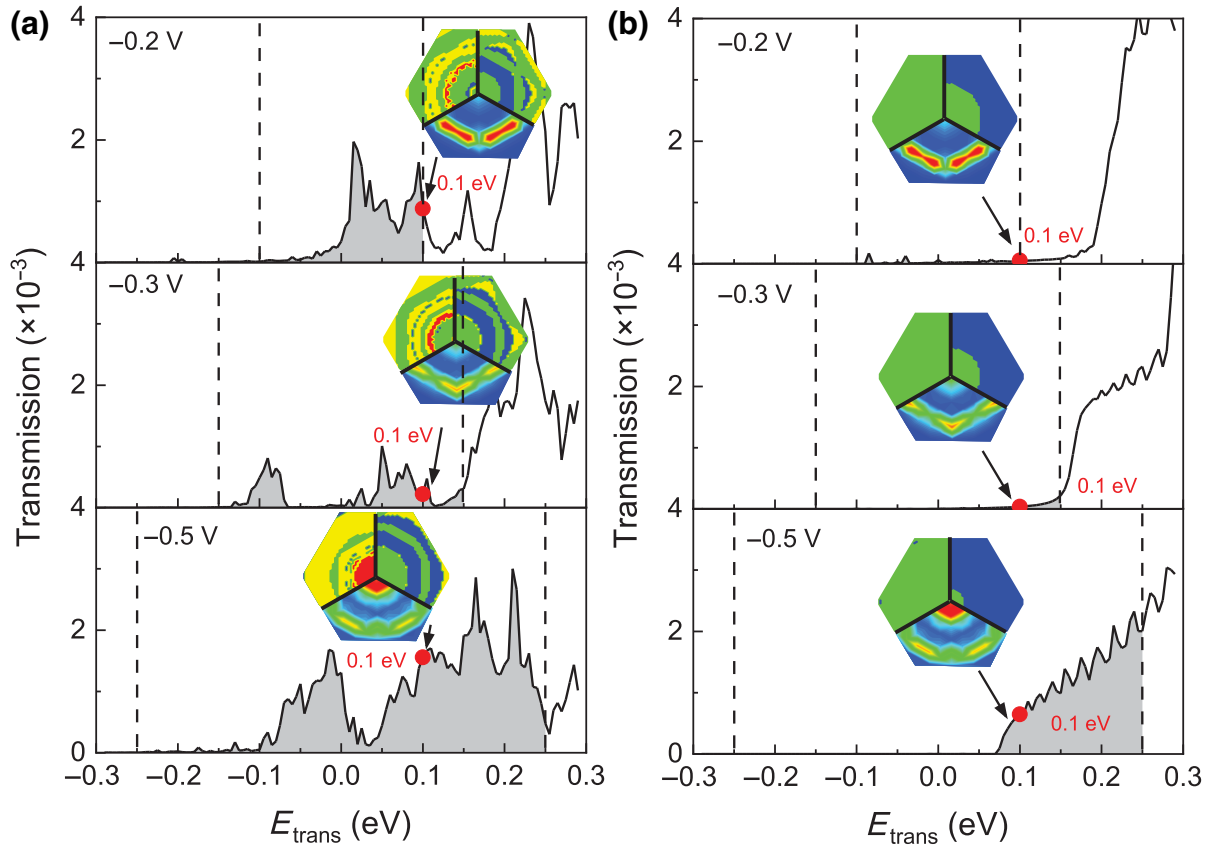


FIG. 5. (a) Majority-spin and (b) minority-spin transmission coefficients of the P configuration as a function of energy under different bias voltages for the AFEH state, respectively. Insets depict the k -resolved spin-dependence channels-DOS figure under bias voltage at the energy point $E = 0.1$ eV. The color bars of channels-DOS figure in insets are same with those in Fig. 2. The vertical dash lines represent the bias voltage window.

wave vector of electrons are conserved in the transmission process.

We further investigate the spin-dependent transport properties of the FGT/BN/IS/BN/FGT vdW AFMFTJ at bias voltage. Figure 3 shows the bias voltage dependences of calculated currents of the FGT/BN/IS/BN/FGT vdW AFMFTJ for all resistance states. As can be seen from Fig. 3, the FGT/BN/IS/BN/FGT vdW AFMFTJ possess the obvious spin-filtering effect over a relatively large bias range in the AFEH state. Correspondingly, when the bias voltage is in the range of -0.2 to 0.2 V, the majority-spin current of the P configuration obviously increases as the bias increases, while the minority-spin current of the P configuration almost remains unchanged with a small value, as shown in Fig. 3(a). For the AP configuration, the majority-spin (minority-spin) currents for the AFEH state are produced only at negative (positive) bias voltage when the bias voltage is in the range of -0.3 to 0.3 V. Interestingly, it is seen from Fig. 3 that whether the magnetic moment of two electrodes is in the AP or P configuration, the total currents for both AFET and AFEH states first increase with the increases of voltage, decrease

with the further increase of the bias voltage after reaching the highest value at -0.2 V bias voltage, and then increase again with the increases of voltage when the voltage is greater than about -0.3 V, indicating that an apparent NDC effect exists in the FGT/BN/IS/BN/FGT vdW AFMFTJ for the AFET and AFEH states when the bias voltage is reversed, as shown in Fig. 3. Meanwhile, the dI_{total}/dV spectra in Figs. 3(d) and 3(h) clearly reproduce the found NDC behavior in the FGT/BN/IS/BN/FGT vdW AFMFTJ for the AFET and AFEH states. It is worth noting that the NDC effect is different for different magnetic configurations and different dipole-ordering states and the NDC effect is the most obvious for the P configuration in the AFET state, thus the NDC effect in this vdW AFMFTJ can be modulated by applying electric field and magnetic field.

According to the Landauer-Büttiker formula, the currents of the FGT/BN/IS/BN/FGT vdW AFMFTJ at bias voltage V are proportional to the integrate transmission coefficients with respect to energies in the bias window

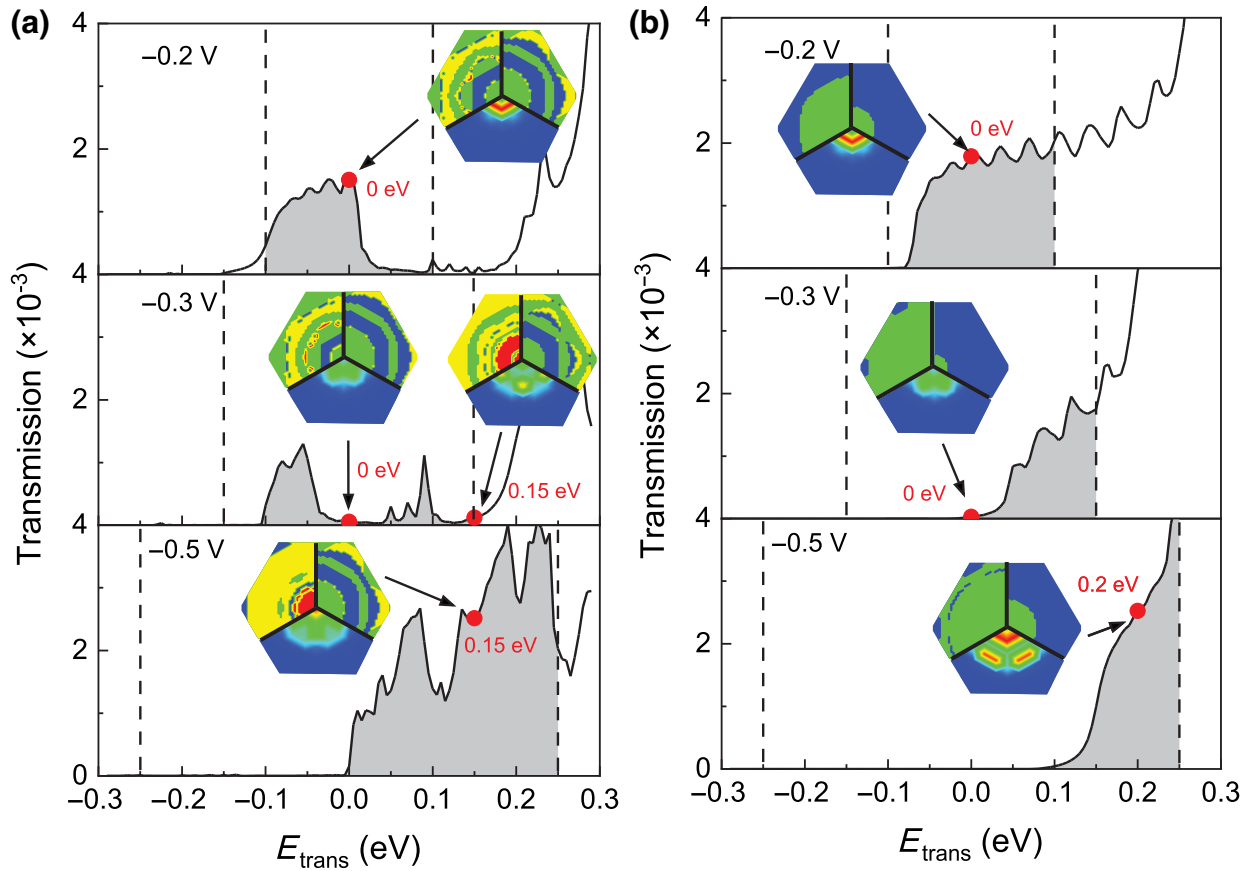


FIG. 6. (a) Majority-spin and (b) minority-spin transmission coefficients of the P configuration as a function of energy under different bias voltages for the AFET state, respectively. Insets depict the k -resolved spin-dependence channels-DOS figure under bias voltage at at different energy point. The color bars of channels-DOS figure in insets are same with those in Fig. 2. The vertical dashed lines represent the bias-voltage window.

ranging from $E_F - eV/2$ to $E_F + eV/2$. Here we first clarify the NDC effect in the FGT/BN/IS/BN/FGT vdW AFMFTJ for the P configuration of the AFEH state by analyzing the transmission coefficients as a function of energy at different bias voltages. Figures 5(a) and 5(b) show that the majority-spin and minority-spin transmission coefficients of the P configuration as a function of energy at different bias voltages for the AFEH state, respectively. It is seen from Fig. 5(a) that when the voltage is equal to -0.2 V, there are some majority-spin transmission peaks in the energy range of 0 to 0.1 eV, and the overall height of these peaks decrease a lot at -0.3 V bias voltage, and then they increase again when the voltage increases to -0.5 V. Taking the transmission at the energy point $E = 0.1$ eV as an example, we analyze the variation of the transmission with bias voltage. As known, the chemical potential of the Ele 1 and Ele 2 at bias voltage V moves to $E_F - eV/2$ and $E_F + eV/2$, respectively, shown in Fig. 4. Therefore, when bias $-V$ is applied to the vdW AFMFTJ, k -resolved spin-dependence channels-DOS figure at $E = 0.1$ eV shown in the inset of Fig. 5(a) is composed of k -resolved spin-dependence conductive channel of Ele 1 at $E = -eV/2 +$

0.1 eV, k -resolved spin-dependence conductive channel of Ele 2 at $E = eV/2 + 0.1$ eV, and k -resolved DOS of In_2Se_3 layer at $E = 0.1$ eV. It is seen from the inset of Fig. 5(a) that when the voltage is equal to -0.2 V, a high majority-spin transmission at $E = 0.1$ eV is mainly attributed to the overlap of the annular region of electronic states of the In_2Se_3 barrier and the nonzero majority-spin conductive channels of two Fe_3GeTe_2 electrodes in the 2DBZ at -0.2 V bias voltage, while significant decrease of the electronic states at the annular region of In_2Se_3 barrier at -0.3 V bias voltage results in lower majority-spin transmission at $E = 0.1$ eV. When the bias increases to -0.5 V, all of the majority-spin conductive channel of Ele 1 and the electronic states of In_2Se_3 barrier obviously increase in the circular region centered at the Γ point, and the large electronic states of the In_2Se_3 barrier, large majority-spin conductive channels of Ele 1 and the nonzero majority-spin conductive channels of Ele 2 overlap in the circular region centered at the Γ point, which results in the increase of the majority-spin transmission at $E = 0.1$ eV again. Meanwhile, the number of majority-spin transmission peaks in the bias window increase with increasing bias

voltage from -0.3 to -0.5 V, as shown in Fig. 5(a). Therefore, the majority-spin current for the P configuration of the AFEH state first increases with the increase of bias voltage, decreases with the further increase of the bias voltage after reaching the highest value at -0.2 V bias voltage, and then increases again with the increases of voltage when the voltage is greater than about -0.3 V, just as shown in Fig. 3(a), resulting an apparent NDC effect. In contrast, insets of Fig. 5(b) show that when the voltage is less than -0.3 V, the annular region of electronic states of In_2Se_3 barrier and the minority-spin nonzero conductive channels of Ele 2 do not overlap for the P configuration of the AFEH state and the large electronic states of In_2Se_3 barrier and the nonzero minority-spin conductive channels of Ele 1 and Ele 2 overlap in the circular region centered at the Γ point when the bias voltage increases to -0.5 V. Correspondingly, when the bias voltage is less than -0.3 V, the minority-spin transmission of the P configuration at $E = 0.1$ eV remains unchanged with a small value while it obviously increases with the voltage increase from -0.3 to -0.5 eV. Also, Fig. 5(b) shows that the number of minority-spin transmission peaks in the bias window increase with increasing bias voltage from -0.3 to -0.5 V. Therefore, the minority-spin current of the P configuration for the AFEH state almost remains unchanged with a small value until the voltage increases to -0.3 eV and it increases with the voltage increase from -0.3 to -0.5 eV, which means that the NDC effect is not produced by the minority-spin current. As a result, the obvious NDC effect in the FGT/BN/IS/BN/FGT vdW AFMFTJ for the P configuration of the AFEH state is produced by the majority-spin current.

Next we clarify the NDC effect in the FGT/BN/IS/BN/FGT vdW AFMFTJ for the P configuration of the AFET state. As shown in Fig. 6(a) [Fig. 6(b)], when the voltage is equal to -0.2 V, the large electronic states of In_2Se_3 barrier and nonzero majority-spin (minority-spin) conductive channels of Ele 1 and Ele 2 overlap in the circular region centered at the Γ point, which causes a high majority-spin (minority-spin) transmission at $E = 0$ eV under -0.2 V bias voltage, while significant decrease of the electronic states of In_2Se_3 barrier in the circular region centered at the Γ point under -0.3 V bias voltage results in a significant low majority-spin (minority-spin) transmission at $E = 0$ eV. It is seen from Fig. 6(a) [Fig. 6(b)] that the height of the majority-spin (minority-spin) transmission peaks in the bias window increase with increasing bias voltage from -0.3 to -0.5 V. Consequently, both of the majority-spin and minority-spin currents for the P configuration of the AFET state first increase with the increase of bias voltage, decrease with the further increase of the bias voltage after reaching the highest value at -0.2 V bias voltage, and then increase again with the increases of voltage when the voltage is greater than about -0.3 V, as shown in Fig. 3(b), which results in a more pronounced NDC effect than that for the P configuration of the AFEH state.

IV. CONCLUSIONS

In conclusion, multiple resistance states can be realized in the FGT/BN/IS/BN/FGT vdW AFMFTJ and the considerable TER ratio of about $1.0 \times 10^4\%$ and the large TMR ratio of up to 695% are simultaneously achieved at zero bias. Moreover, whether the magnetic moment of two electrodes is in the AP or P configuration, the total currents for both AFET and AFEH states first increase with the increases of voltage, decrease with the further increase of the bias voltage after reaching the highest value at -0.2 V bias voltage, and then increase again with the increases of voltage when the voltage is greater than about -0.3 V, resulting an apparent NDC effect in the FGT/BN/IS/BN/FGT vdW AFMFTJ for the AFET and AFEH states. Interestingly, the NDC effect in this vdW AFMFTJ can be modulated by applying electric field and magnetic field. Our results provide a promising avenue for simultaneous realization of the large TER and TMR ratios and the regulatable NDC effect in the multifunctional microelectronic devices.

ACKNOWLEDGMENTS

This work was financial supported by the National Key Research and Development Program of China [MOST Grant No. 2022YFA1402800], the National Natural Science Foundation of China [NSFC, Grants No. 51831012, No. 12134017, No. 12204517, and No. 12274175], and partially supported by the Strategic Priority Research Program (B) [Grant No. XDB33000000] and Beijing Natural Science Foundation (Grant No. Z201100004220006). The atomic structures were produced using VESTA software [49]. The work was carried out at National Supercomputer Center in Tianjin, and the calculations were performed on TianHe-1 (A).

-
- [1] H. Lin, F. Yan, C. Hu, Q. Lv, W. Zhu, Z. Wang, Z. Wei, K. Chang, and K. Wang, Spin-Valve Effect in $\text{Fe}_3\text{GeTe}_2/\text{MoS}_2/\text{Fe}_3\text{GeTe}_2$ van der Waals Heterostructures, *ACS Appl. Mater. Interfaces* **12**, 43921 (2020).
 - [2] C. Hu, F. Yan, Y. Li, and K. Wang, Vertical WS_2 spin valve with Ohmic property based on Fe_3GeTe_2 electrodes, *Chin. Phys. B* **30**, 097505 (2021).
 - [3] H. Lin, X. Luo, L. Liu, D. Wang, X. Zhao, Z. Wang, X. Xue, F. Zhang, and G. Xing, All-electrical control of compact SOT-MRAM: Toward highly efficient and reliable non-volatile in-memory computing, *Micromachines* **13**, 319 (2022).
 - [4] T. H. Kim, J. Lee, R.-G. Lee, and Y.-H. Kim, Gate- versus defect-induced voltage drop and negative differential resistance in vertical graphene heterostructures, *npj Comput. Mater.* **8**, 50 (2022).
 - [5] C. Liu, H. Chen, X. Hou, H. Zhang, J. Han, Y.-G. Jiang, X. Zeng, D. W. Zhang, and P. Zhou, Small footprint transistor

- architecture for photoswitching logic and in situ memory, *Nat. Nanotechnol.* **14**, 662 (2019).
- [6] B. Fallahazad, K. Lee, S. Kang, J. Xue, S. Larentis, C. Corbet, K. Kim, H. C. P. Movva, T. Taniguchi, K. Watanabe, L. F. Register, S. K. Banerjee, and E. Tutuc, Gate-tunable resonant tunneling in double bilayer graphene heterostructures, *Nano Lett.* **15**, 428 (2015).
- [7] A. Mishchenko, *et al.*, Twist-controlled resonant tunnelling in graphene/boron nitride/graphene heterostructures, *Nat Nanotechnol.* **9**, 808 (2014).
- [8] B. Huang, G. Clark, E. Navarro-Moratalla, D. R. Klein, R. Cheng, K. L. Seyler, D. Zhong, E. Schmidgall, M. A. McGuire, D. H. Cobden, W. Yao, D. Xiao, P. Jarillo-Herrero, and X. Xu, Layer-dependent ferromagnetism in a van der Waals crystal down to the monolayer limit, *Nature* **546**, 270 (2017).
- [9] C. Gong, L. Li, Z. Li, H. Ji, A. Stern, Y. Xia, T. Cao, W. Bao, C. Wang, Y. Wang, Z. Q. Qiu, R. J. Cava, S. G. Louie, J. Xia, and X. Zhang, Discovery of intrinsic ferromagnetism in two-dimensional van der Waals crystals, *Nature* **546**, 265 (2017).
- [10] Y. Deng, Y. Yu, Y. Song, J. Zhang, N. Z. Wang, Z. Sun, Y. Yi, Y. Z. Wu, S. Wu, J. Zhu, J. Wang, X. H. Chen, and Y. Zhang, Gate-tunable room-temperature ferromagnetism in two-dimensional Fe_3GeTe_2 , *Nature* **563**, 94 (2018).
- [11] F. Liu, L. You, K. L. Seyler, X. Li, P. Yu, J. Lin, X. Wang, J. Zhou, H. Wang, H. He, S. T. Pantelides, W. Zhou, P. Sharma, X. Xu, P. M. Ajayan, J. Wang, and Z. Liu, Room-temperature ferroelectricity in CuInP_2S_6 ultrathin flakes, *Nat. Commun.* **7**, 12357 (2016).
- [12] Y. Zhou, D. Wu, Y. Zhu, Y. Cho, Q. He, X. Yang, K. Herrera, Z. Chu, Y. Han, M. C. Downer, H. Peng, and K. Lai, Out-of-plane piezoelectricity and ferroelectricity in layered $\alpha\text{-In}_2\text{Se}_3$ nanoflakes, *Nano Lett.* **17**, 5508 (2017).
- [13] X. Cai, T. Song, N. P. Wilson, G. Clark, M. He, X. Zhang, T. Taniguchi, K. Watanabe, W. Yao, D. Xiao, M. A. McGuire, D. H. Cobden, and X. Xu, Atomically thin CrCl_3 : An in-plane layered antiferromagnetic insulator, *Nano Lett.* **19**, 3993 (2019).
- [14] Z. Wang, D. Sapkota, T. Taniguchi, K. Watanabe, D. Mandrus, and A. F. Morpurgo, Tunneling spin valves based on $\text{Fe}_3\text{GeTe}_2/\text{hBN}/\text{Fe}_3\text{GeTe}_2$ van der Waals heterostructures, *Nano Lett.* **18**, 4303 (2018).
- [15] D. R. Klein, D. MacNeill, J. L. Lado, D. Soriano, E. Navarro-Moratalla, K. Watanabe, T. Taniguchi, S. Manni, P. Canfield, J. Fernández-Rossier, and P. Jarillo-Herrero, Probing magnetism in 2D van der Waals crystalline insulators via electron tunneling, *Science* **360**, 1218 (2018).
- [16] T. Song, Z. Fei, M. Yankowitz, Z. Lin, Q. Jiang, K. Hwangbo, Q. Zhang, B. Sun, T. Taniguchi, K. Watanabe, M. A. McGuire, D. Graf, T. Cao, J.-H. Chu, D. H. Cobden, C. R. Dean, D. Xiao, and X. Xu, Switching 2D magnetic states via pressure tuning of layer stacking, *Nat. Mater.* **18**, 1298 (2019).
- [17] Y. Feng, X. Wu, L. Hu, and G. Gao, $\text{FeCl}_2/\text{MoS}_2/\text{FeCl}_2$ van der Waals junction for spintronic applications, *J. Mater. Chem. C* **8**, 14353 (2020).
- [18] J. Wu, H.-Y. Chen, N. Yang, J. Cao, X. Yan, F. Liu, Q. Sun, X. Ling, J. Guo, and H. Wang, High tunnelling electroresistance in a ferroelectric van der Waals heterojunction via giant barrier height modulation, *Nat. Electron.* **3**, 466 (2020).
- [19] L. Kang, P. Jiang, H. Hao, Y. Zhou, X. Zheng, L. Zhang, and Z. Zeng, Giant tunneling electroresistance in two-dimensional ferroelectric tunnel junctions with out-of-plane ferroelectric polarization, *Phys. Rev. B* **101**, 014105 (2020).
- [20] Y. Yang, L. Zhang, J. Chen, X. Zheng, L. Zhang, L. Xiao, and S. Jia, An electrically switchable anti-ferroelectric bilayer In_2Se_3 based opto-spintronic device, *Nanoscale* **13**, 8555 (2021).
- [21] J. Ding, D.-F. Shao, M. Li, L.-W. Wen, and E. Y. Tsymlal, Two-Dimensional Antiferroelectric Tunnel Junction, *Phys. Rev. Lett.* **126**, 057601 (2021).
- [22] H. Bai, X. Li, H. Pan, P. He, Z.-a. Xu, and Y. Lu, van der Waals antiferroelectric magnetic tunnel junction: A first-principles study of a $\text{CrSe}_2/\text{CuInP}_2\text{S}_6/\text{CrSe}_2$ junction, *ACS Appl. Mater. Interfaces* **13**, 60200 (2021).
- [23] Z. Yan, Z. Li, Y. Han, Z. Qiao, and X. Xu, Giant tunneling magnetoresistance and electroresistance in $\alpha\text{-In}_2\text{Se}_3$ -based van der Waals multiferroic tunnel junctions, *Phys. Rev. B* **105**, 075423 (2022).
- [24] Y. Chen, Z. Tang, M. Dai, X. Luo, and Y. Zheng, Giant magnetoresistance and tunneling electroresistance in multiferroic tunnel junctions with 2D ferroelectrics, *Nanoscale* **14**, 8849 (2022).
- [25] S. Liu, X. Yuan, Y. Zhou, Y. Sheng, C. Huang, E. Zhang, J. Ling, Y. Liu, W. Wang, C. Zhang, J. Zou, K. Wang, and F. Xiu, Wafer-scale two-dimensional ferromagnetic Fe_3GeTe_2 thin films were grown by molecular beam epitaxy, *npj 2D Mater. Appl.* **1**, 1 (2017).
- [26] B. Lv, Z. Yan, W. Xue, R. Yang, J. Li, W. Ci, R. Pang, P. Zhou, G. Liu, Z. Liu, W. Zhu, and X. Xu, Layer-dependent ferroelectricity in 2H-stacked few-layer $\alpha\text{-In}_2\text{Se}_3$, *Mater. Horiz.* **8**, 1472 (2021).
- [27] C. Cui, W.-J. Hu, X. Yan, C. Addiego, W. Gao, Y. Wang, Z. Wang, L. Li, Y. Cheng, P. Li, X. Zhang, H. N. Alsharief, T. Wu, W. Zhu, X. Pan, and L.-J. Li, Intercorrelated in-plane and out-of-plane ferroelectricity in ultrathin two-dimensional layered semiconductor In_2Se_3 , *Nano Lett.* **18**, 1253 (2018).
- [28] L. Esaki, New phenomenon in narrow germanium p-n junctions, *Phys. Rev.* **109**, 603 (1958).
- [29] J. Chen, M. A. Reed, A. M. Rawlett, and J. M. Tour, Large on-off ratios and negative differential resistance in a molecular electronic device, *Science* **286**, 1550 (1999).
- [30] Q. Li, C. Jia, Y. Ren, Y. Zhang, and W. Zhang, Negative pulse and compliance current dependent negative differential resistance in $\text{ZnO}/\text{Nb}:\text{SrTiO}_3$ heterojunctions, *Phys. Status Solidi A* **218**, 2000715 (2021).
- [31] Y. Wu, D. B. Farmer, W. Zhu, S.-J. Han, C. D. Dimitrakopoulos, A. A. Bol, P. Avouris, and Y.-M. Lin, Three-terminal graphene negative differential resistance devices, *ACS Nano* **6**, 2610 (2012).
- [32] D. Li, Y. Tong, K. Bairagi, M. Kelai, Y. J. Dappe, J. Lagoute, Y. Girard, S. Rousset, V. Repain, C. Barretau, M. Brandbyge, A. Smogunov, and A. Bellec, Negative differential resistance in spin-crossover molecular devices, *J. Phys. Chem. Lett.* **13**, 7514 (2022).

- [33] J. Liu and D. Segal, Sharp negative differential resistance from vibrational mode softening in molecular junctions, *Nano Lett.* **20**, 6128 (2020).
- [34] L.-J. Yin, L.-Z. Yang, L. Zhang, Q. Wu, X. Fu, L.-H. Tong, G. Yang, Y. Tian, L. Zhang, and Z. Qin, Imaging of nearly flat band induced atomic-scale negative differential conductivity in ABC-stacked trilayer graphene, *Phys. Rev. B* **102**, 241403(R) (2020).
- [35] S.-Y. Li, H. Liu, J.-B. Qiao, H. Jiang, and L. He, Magnetic-field-controlled negative differential conductance in scanning tunneling spectroscopy of graphene NPN junction resonators, *Phys. Rev. B* **97**, 115442 (2018).
- [36] L. Britnell, R. V. Gorbachev, A. K. Geim, L. A. Ponomarenko, A. Mishchenko, M. T. Greenaway, T. M. Fromhold, K. S. Novoselov, and L. Eaves, Resonant tunnelling and negative differential conductance in graphene transistors, *Nat. Commun.* **4**, 1794 (2013).
- [37] G. Kresse and J. Hafner, Ab initio molecular dynamics for liquid metals, *Phys. Rev. B* **47**, 558 (1993).
- [38] G. Kresse and J. Furthmüller, Efficient iterative schemes for ab initio total-energy calculations using a plane-wave basis set, *Phys. Rev. B* **54**, 11169 (1996).
- [39] P. E. Blöchl, Projector augmented-wave method, *Phys. Rev. B* **50**, 17953 (1994).
- [40] J. P. Perdew, K. Burke, and M. Ernzerhof, Generalized Gradient Approximation Made Simple, *Phys. Rev. Lett.* **77**, 3865 (1996).
- [41] J. c. v. Klimeš, D. R. Bowler, and A. Michaelides, van der Waals density functionals applied to solids, *Phys. Rev. B* **83**, 195131 (2011).
- [42] J. Taylor, H. Guo, and J. Wang, Ab initio modeling of open systems: Charge transfer, electron conduction, and molecular switching of a C_{60} device, *Phys. Rev. B* **63**, 121104(R) (2001).
- [43] J. Taylor, H. Guo, and J. Wang, Ab initio modeling of quantum transport properties of molecular electronic devices, *Phys. Rev. B* **63**, 245407 (2001).
- [44] S. Yuan, W. F. Io, J. Mao, Y. Chen, X. Luo, and J. Hao, Enhanced piezoelectric response of layered In_2Se_3/MoS_2 nanosheet-based van der Waals heterostructures, *Acs Appl Nano Mater.* **3**, 11979 (2020).
- [45] S. Popović, B. Čelustka, and D. Bidjin, X-ray diffraction measurement of lattice parameters of In_2Se_3 , *Phys. Stat. Sol. (a)* **6**, 301 (1971).
- [46] H.-J. Deiseroth, K. Aleksandrov, C. Reiner, L. Kienle, and R. K. Kremer, Fe_3GeTe_2 and Ni_3GeTe_2 – two new layered transition-metal compounds: Crystal structures, HRTEM investigations, and magnetic and electrical properties, *Eur. J. Inorg. Chem* **2006**, 1561 (2006).
- [47] Y.-N. Xu and W. Y. Ching, Electronic, optical, and structural properties of some wurtzite crystals, *Phys. Rev. B* **48**, 4335 (1993).
- [48] X. Li, J.-T. Lü, J. Zhang, L. You, Y. Su, and E. Y. Tsybal, Spin-dependent transport in van der Waals magnetic tunnel junctions with Fe_3GeTe_2 electrodes, *Nano Lett.* **19**, 5133 (2019).
- [49] K. Momma and F. Izumi, VESTA3 for three-dimensional visualization of crystal, volumetric and morphology data, *J. Appl. Cryst.* **44**, 1272 (2011).